JOURNAL OF SPACECRAFT AND ROCKETS
Vol. 41, No. 2, March–April 2004

Improving Metallic Thermal Protection System Hypervelocity Impact Resistance Through Numerical Simulations

Carl C. Poteet* and Max L. Blosser†
NASA Langley Research Center, Hampton, Virginia 23681

A design of experiments approach has been implemented using computational hypervelocity impact simulations. The purpose of this study is to determine the most effective place to make minor design changes to an existing metallic thermal protection system to improve hypervelocity impact protection provided to underlying components. Simulations are performed using axisymmetric models in a shock-physics hydrodynamics code and compared with existing experimental data. The axisymmetric models are then used in a statistical sensitivity analysis to determine the influence of design parameters on degree of protection. Several damage metrics are identified and evaluated. Damage metrics related to the extent of substructure damage produce misleading results; however, damage metrics related to the degree of dispersion of the hypervelocity projectile produce results that correspond to physical intuition. Based on analysis of variance results, it is concluded that increasing the spacing between the outer surface and the substructure is the most effective way to increase hypervelocity impact resistance. The second most effective design change is to increase the thickness of the outer foil layer. When design considerations are taken into account for the system in this study, it is explained that increasing the thickness of the outer foil layer is the most practical design change.

Nomenclature

A	=	annulus cross-sectional area, cm^2
F	=	variance ratio
L	=	axial momentum, g · cm/s
L_{annular}	=	annular momentum per unit area, g/cm · s
ε	=	error associated with analysis of means additive approximation, cm
η	=	response, from analysis of means, cm

Introduction

HYPERVELOCITY impact resistance is an important design consideration for metallic thermal protection systems (TPS) proposed for future reusable launch vehicles. The impact velocity between orbiting particles (space debris and micrometeoroids) and orbiting vehicles is typically in excess of material sound speed, resulting in the term hypervelocity impact. The average relative velocity between space debris and orbiting vehicles is 10 km/s, but can be as high as 16 km/s. At these velocities, even small particles have sufficient energy to damage a spacecraft significantly. Metallic TPS may cover a large percentage of the vehicle exterior surface, resulting in increased probability over the vehicle design life of impact with particles large enough to penetrate the TPS. Penetration of the TPS may decrease the level of thermal protection provided on reentry, and the impact debris may also damage components (fuel tank, crew cabin, structural members, etc.) underneath the TPS.

A review of metallic TPS development evolution is included in Ref 1. Several of the more recently developed metallic TPS concepts include a foil-gauge honeycomb sandwich on the TPS outer, aerodynamic surface and a inner foil layer on the inner surface that together with foil side walls encapsulate several centimeters of fibrous insulation. Figure 1 shows the metallic TPS concept examined. The TPS is mechanically attached to underlying components. Computational results are compared to experimental results in which attachment is to a 0.254-cm-thick aluminum 2024-T81 plate representative of the space shuttle aluminum substructure. Material selection for the TPS outer honeycomb sandwich depends on thermal and mechanical conditions present during the flight cycle of the reusable launch vehicle, where design considerations include peak reentry surface temperature, oxidation, creep, and pressure loading expected at the TPS mounting location. Inconel 617 and Ti–6Al–4V outer honeycomb sandwich materials are examined in this study. Inconel 617 has been identified as a viable material for use in the outer honeycomb sandwich for vehicle regions that experience peak temperatures between 600 and 980°C during reentry. In regions experiencing peak temperatures lower than 600°C, Ti–6Al–4V is a candidate material. The inner foil layer, comprising the back of the TPS panel, experiences lower temperatures and is made of Ti–6Al–4V for all vehicle regions.

The configuration of the metallic TPS design in the center of a panel, away from the edges and attachments, is very similar to a Whipple shield,[2] a structure used to protect satellites from space debris. As shown in Fig. 2, the basic Whipple shield design consists of one or more thin walls separated by a standoff distance from the structure being protected. The center of a TPS panel (excluding the fibrous insulation and honeycomb core) is similar to a Whipple shield, consisting of three thin-foil layers with spacing between them. Therefore, the TPS panel may already be in a good configuration to shield against orbital debris. With modification of key design parameters, it may be possible to enhance impact protection significantly.

The objective of this study is to identify, at a preliminary design level, the most mass efficient way to modify an existing metallic TPS to improve the impact protection provided to underlying components. The improved TPS design must still meet the requirements and constraints imposed by the launch vehicle it is mounted on. The design requirements significantly limit the wall thicknesses that can be used because launch vehicles are extremely weight critical. Launch vehicle design considerations also limit the total standoff distance that can be used because increasing TPS thickness increases the overall vehicle size, adversely affecting vehicle weight and performance. These vehicle level design issues will be considered when selecting design parameter levels in the statistical analysis and when determining the best design changes to improve hypervelocity impact protection.

A given TPS design can potentially be attached over many types of components, composed of different materials, thicknesses, standoff,

Received 28 May 2002; accepted for publication 16 July 2003.

*Research Engineer, Metals and Thermal Structures Branch, Structures and Materials Competency, Mail Stop 396.

†Senior Research Engineer, Metals and Thermal Structures Branch, Structures and Materials Competency, Mail Stop 396.

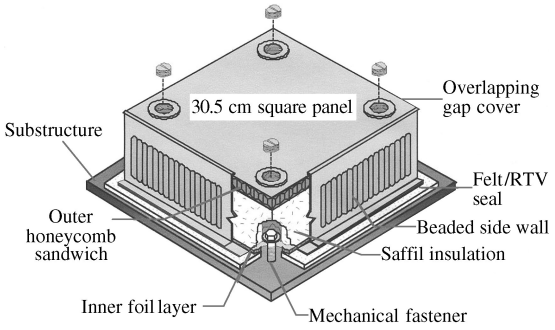

Fig. 1 Metallic TPS panel mounted on substructure.

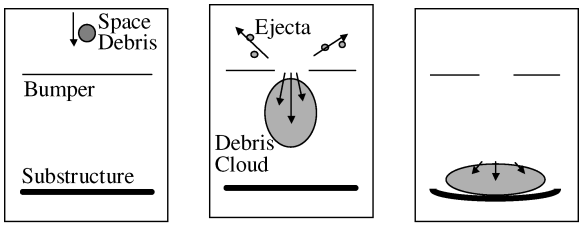

a) Space debris approaches spacecraft

b) Debris impacts bumper layer and disperses

c) Dispersed debris cloud spread over wide area

Fig. 2 Basic Whipple shield design principle.

and tolerance to damage. The design of both the TPS and the underlying component are important in determining penetration and damage from hypervelocity impact and should be considered for a detailed final design. This study, however, is undertaken at a preliminary design level, focusing only on the TPS design, and the ability of the TPS design to disperse effectively the hypervelocity projectile. A well-dispersed projectile should be less of a threat to any of the potential components to which metallic TPS will be attached.

The approach taken was to first generate computational models of hypervelocity impact on metallic TPS panels. Two configurations of TPS were selected for modeling, one with an Inconel 617 outer honeycomb sandwich and the other with a Ti–6Al–4V outer honeycomb sandwich. Both computational models correspond to configurations tested in Ref. 3. Comparison is made with the experimental results. Then, the TPS with Inconel 617 outer honeycomb sandwich is used in a statistical sensitivity study that varies five TPS design parameters to identify design changes that will improve impact protection provided to underlying components.

Experimental Results

In a previous effort,[3] 33 experimental hypervelocity impact tests were performed on various metallic TPS configurations using the NASA Marshall Space Flight Center Orbital Debris Simulation Facility. All tests were with either 0.318-, 0.476-, or 0.635-cm spherical 1100-O aluminum projectiles fired normal to the TPS surface, with velocities ranging from 7.0 to 7.9 km/s. There were 20 tests with the TPS design studied in this paper. Figure 1 shows a schematic of the primary features of the TPS design.

Figure 3a shows a cutaway view through the center of the TPS panel shown in Fig 1. In the experiments, the facesheets and honeycomb core of the outer honeycomb sandwich panel were composed of either Inconel 617 or Ti–6Al–4V, with facesheet thicknesses ranging from $6.35E{-}3$ cm to $2.54E{-}2$ cm and $7.62E{-}3$ cm to $3.56E{-}2$ cm, respectively. Two different honeycomb core cell sizes were examined for the Inconel 617 outer honeycomb sandwich, either 0.476 or 0.635 cm, but only the 0.476-cm core was examined for Ti–6Al–4V outer honeycomb sandwich. Honeycomb ribbon gauge was dependent on cell size: Honeycomb cell size of 0.476 cm used $3.81E{-}3$ cm gauge ribbon; honeycomb cell size of 0.635 cm used $5.08E{-}3$ cm gauge ribbon. The insulation layer was

Table 1 Experimental parameters

Parameter	Specimen 6	Specimen 17
Projectile		
Material	1100–O Al	1100–O Al
Velocity, km/s	7.5	7.1
Diameter, cm	0.476	0.476
Outer facesheet		
Material	INC617	Ti–6Al–4V
Gauge, cm	0.0127	0.0127
Honeycomb core		
Material	INC617	Ti–6Al–4V
Cell size, cm	0.635	0.476
Gauge, cm	$5.08E{-}03$	$3.81E{-}03$
Depth, cm	0.711	0.711
Inner facesheet		
Material	INC617	Ti–6Al–4V
Gauge, cm	0.0127	0.0127
Insulation		
Material	Saffil	Saffil
Thickness, cm	5.08	5.08
Approximate density, g/cm^3	0.0233	0.0233
Titanium foil		
Material	Ti–6Al–4V	Ti–6Al–4V
Gauge, cm	$7.62E{-}03$	$7.62E{-}03$
Substructure		
Material	2024–T81 Al	2024-T81 Al
Thickness, cm	0.254	0.254

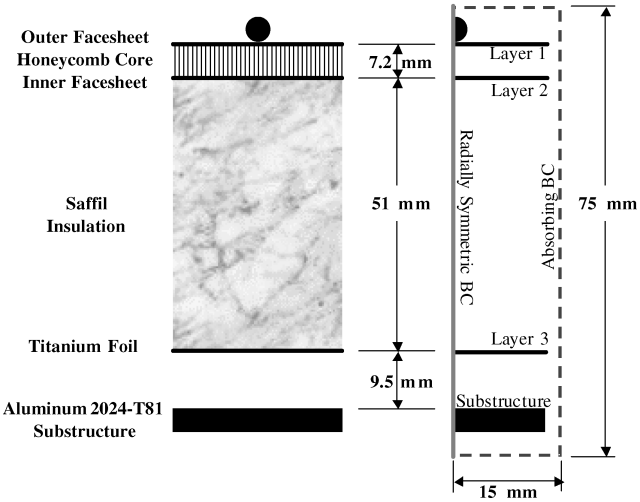

a) Experimental configuration

b) Axisymmetric computational model

Fig. 3 Comparison of experimental TPS configuration (through the thickness) to axisymmetric computational model.

composed of Saffil™ alumina-based fibrous insulation. Density of tested insulation layers were estimated to be between 0.0203 and 0.0263 g/cm^3, and in most test cases, the insulation layer was 5.08 cm thick. In tests with the configuration of Figs. 1 and 3, the inner foil layer was $7.72E{-}3$ cm thick Ti–6Al–4V foil, and spacing between the inner foil layer and the substructure was 0.95 cm. The substructure was 0.254-cm-thick aluminum 2024-T81 plate, representative of the space shuttle substructure.

Two particular test cases were selected for comparison with computational hypervelocity impact simulations: specimen 6, which uses an Inconel 617 outer honeycomb sandwich, and specimen 17, which uses a Ti–6Al–4V outer honeycomb sandwich. Experimental parameters for both specimens are listed in Table 1. Specimens were chosen that had outer facesheet parameters in a desirable range when other factors, such as weight, structural requirements, and low-speed impact damage from hail and flying through rain were considered. Both of these cases use a 0.476-cm-diam projectile. From the experiments, it was found that most of the TPS configurations tested

prevent substructure penetration from 0.318-cm-diam projectiles. All tests with larger 0.635-cm-diam projectiles result in penetration of the TPS and substructure, and it was clear from the level of damage that significant modification of the TPS would be required to provide protection against a projectile of this size. However, substructure damage in tests with the 0.476-cm-diam projectile was sensitive to changes in TPS parameters, making this projectile size interesting for study in a sensitivity analysis.

Testing of specimens 6 and 17 resulted in penetration of the TPS panel and substructure. Details of the damage to the substructure will be given in the section "Comparison with Experimental Results." For complete data from the experiments, see Ref. 3.

Method

In this study, computational models are developed of a simplified TPS configuration, representative of the center of a metallic TPS panel. Two models are created, the first for TPS with Ti–6Al–4V outer honeycomb sandwich panel and the second for TPS with Inconel 617 outer honeycomb sandwich panel. Damage predicted using the first and second models are compared to experimental specimens 17 and 6, respectively, reported in Ref. 3. Experimental parameters are listed in Table 1. The Inconel 617 model is then used in a statistical sensitivity analysis to quantify and rank influences of key design parameters on impact protection provided to underlying components.

Model Description

Two different hypervelocity impact models were generated for comparison with the experimental specimens listed in Table 1. One of these was an all-titanium TPS model for comparison with specimen 17; the other model was of TPS with Inconel 617 outer honeycomb sandwich and a Ti–6Al–4V inner foil layer, for comparison with specimen 6.

Hypervelocity impact models were generated in CTH,[4] a shock-physics code developed at Sandia National Laboratories. CTH can be used to solve problems involving multiple materials, large deformations and strong shocks. A finite volume technique is implemented with an Eulerian mesh to solve the conservation of mass, momentum, and energy equations. Only mechanical effects are considered in this study. Electromagnetic, chemical, and heat conduction effects are neglected.

Figure 3 shows a comparison of the key features of the computational model with the experimental setup. An axisymmetric model was generated to reduce computational time and memory requirements, allowing workstation-class computer resources to be used.

The honeycomb sandwich panel outer facesheet and inner facesheet will be referred to as layer 1 and layer 2, respectively. The honeycomb core between layers 1 and 2 was omitted. To model honeycomb core accurately requires a three-dimensional model. The $3.81E{-}3$–$5.08E{-}3$ thick honeycomb ribbon requires an extremely dense mesh, which would result in model size and runtimes in excess of the capabilities of available computer workstations. Previous computational studies[5] using the same TPS configuration studied in this paper revealed that impact normal to the outer surface at different locations relative to the honeycomb core can produce significantly different responses. Impact in the center of a honeycomb cell was shown to channel the debris cloud, resulting in an increase in debris cloud lethality compared to a TPS panel without honeycomb core. However, impact directly over a junction in the honeycomb ribbon resulted in increased dispersion of the debris cloud and reduced damage to the substructure. In Ref. 5, it was shown that the level of debris cloud dispersion when the honeycomb was omitted was in between that of the cell-centered and junction-centered impact. It would be very informative to study the effect of the honeycomb layer in greater detail, either computationally or experimentally; however, at the preliminary design level it is believed that omission of the honeycomb layer is justified.

The Saffil fibrous insulation layer was neglected because it could not be readily modeled with CTH. The low-density insulation should attenuate the effects of the impacting projectile somewhat, and neglecting the insulation should produce a conservative result. It is assumed that when statistical analysis is performed on the simplified model, design changes identified as increasing the level of protection to underlying components will be beneficial for the case with Saffil as well. However, the effect of Saffil is not well understood. Although it is assumed to be minor, the tests in Ref. 3 do not clearly reveal the influence of the Saffil insulation layer.

The inner foil layer and aluminum substructure were modeled. In discussion of the computational model these layers will be referred to as layer 3 and substructure, respectively.

Table 2 CTH material parameters

Material	EOS	Yield strength, MPa	Fracture strength, MPa
1100–O Al	SESAME aluminum	34	−100
2024–T81 Al	SESAME aluminum	Johnson–Cook	−1500
Ti–6Al–4V	ANEOS Ti–6Al–4V	880	−2860
Inconel 617	ANEOS Ni	350	−1400

Material modeling in CTH can be broken into three categories: volumetric response, resistance to distortion, and failure.[6] Material volumetric response, or resistance to compression, is predicted using an equation of state (EOS). Highly detailed, tabularized EOS are used with CTH that report pressure and energy as a function of density and temperature. The EOS used are valid through the range of densities and temperatures experienced in a hypervelocity impact and account for multiple material phase changes. Material constitutive response for the hypervelocity projectile and TPS layers was modeled with a simple elastic–plastic model with Von Mises yield surfaces. The aluminum substructure was modeled using the more detailed Johnson–Cook viscoplastic model. Failure in tension was modeled using the standard CTH option in which tension is relieved by introducing a void into computational cells when the hydrostatic tensile stress exceeds fracture strength.[7]

Table 2 contains the EOS, yield strength, and fracture strength values used. The SESAME[8] aluminum EOS was used for both Al 1100–O and Al 2024–T81. A density correction factor was used with Al 2024–T81 to account for the lower density due to alloying. A tabularized version of the analytical equation of state (ANEOS)[9] was used for titanium-foil layers. The EOS for Inconel 617 was approximated by using the tabularized ANEOS for nickel with a density correction factor of 1.06 to correct for the density difference. Because Inconel 617 is heavily alloyed, it is unclear what the accuracy of the EOS approximation will be.

Materials in Table 2 with a numerical entry under yield strength use an elastic–plastic model with Von Mises yield surface for material strength. The substructure was modeled using the Johnson–Cook viscoplastic model[9] with default values for 2024-T351 aluminum because no constitutive model was available for 2024-T81. Failure in tension was modeled using the standard CTH option in which tension is relieved by introducing a void into computational cells when the mean principal stress exceeds the fracture strength. The fracture strength for 2024 aluminum is estimated from values for 2219 aluminum given by Hertel.[2] Fracture strength for titanium is derived from the dynamic yield stress reported by Babcock et al.[10] multiplied by a factor of two, as suggested by Silling.[7] Values for the dynamic yield stress of Inconel 617 were not available. However, dynamic yield strength is typically on the order of twice the static yield strength. Fracture strength for Inconel 617 was obtained by multiplying the yield strength[11] by a factor of two (to approximate dynamic yield strength) and then multiplying by an additional factor of two (as suggested by Silling[7]).

Axisymmetric models were generated in which a rectangular mesh of computational cells were created in a radial plane. Thus, each rectangular computational cell represents a cylindrical annulus centered around the axis of symmetry. As shown in Fig. 3, a radially symmetric boundary condition was imposed along the axis of symmetry, preventing mass, momentum, stress deviator, and energy fluxes through the axis of symmetry. Absorbing boundary conditions were used along all other boundaries, allowing material to flow out of the computational domain. Material layers were unrestrained.

Because impact occurs at velocities in excess of material sound speeds, the conditions at the edges of a material layer will not influence the response during the initial microseconds of impact, the time frame of interest.

It is standard practice to use four or more computational cells through the thickness of a layer to allow adequate resolution of the shock structure.[12] In addition, to ensure an accurate computational solution, computational cells should be square in impacted areas and cell dimensions should only be varied gradually. A two-step Eulerian solution scheme is used in CTH that requires that both material and void be meshed. The geometry of the model in this study, with large spacing between relatively thin layers, requires an extremely dense mesh. To make solution of the model on the computer resources available more practical, it was decided to use only two computational cells through the wall thickness, the rationale being that the shock structure in the thin layers may not be captured completely, but that the shock structure generated in the larger, more massive incoming projectile will be generated with reasonable accuracy. In a previous study, it was shown that this assumption was reasonable for problems with this geometry.[5] This reduces the required number of computational cells by a factor of four and total runtime by a factor of five. Runtime is on the order of 1 CPU-day for this modeling scheme, running on an SGI MIPS R10000 CPU.

During a hypervelocity impact simulation, a large amount of low, density gas is generated, which tends to increase computational run time dramatically and may lead to numerical difficulties. To avoid computational problems, a material filter was used to remove material with both density below 0.005 g/cm^3 and pressure below 0.1 MPa. Discarding material of such low density is assumed to have a negligible effect on the simulation.

Comparison with Experimental Results

Figures 4 and 5 show progression of the computational hypervelocity impact simulation of an all-titanium TPS panel, for comparison with results from experimental specimen 17. Except for the omission of the honeycomb layer and Saffil insulation layer, computational simulation parameters were consistent with the experimental parameters listed in Table 1. Figure 4 shows the initial configuration and calculation at 1.00 and 3.00 μs, with results displayed in the vicinity of layers 1 and 2. Layer 1, despite being much thinner than the projectile diameter, has shocked the projectile at 1.0 μs, causing spalling to occur. Spalling is a tensile failure resulting from the reflection of compressive waves at free surfaces. At this point, the debris cloud is composed primarily of high-density fragments arranged in an expanding semispherical pattern. On impact with layer 2, fragments in the leading edge of the debris cloud are shocked again. At 3 μs, a low-density gas region is noticeable in front and to the side of the high-density fragments. The debris cloud high-density core disperses as it travels toward layer 3. Figure 5 shows calculation at 8.75, 10.25, and 12.00 μs, with results displayed in the region of layers 3 and the substructure. At 8.75 μs, contact is made with layer 3, and by 10.25 μs, the debris cloud is dispersed considerably. Solid fragments show up in the results as high- (greater than 1000 kg/m^3) density regions and are still noticeable in the debris cloud before substructure impact. At 12 μs, substructure penetration is underway. Solid fragments near the impact centerline are in the process of penetrating the substructure, and overlapping fragments farther from the centerline have resulted in severe cratering. The shock wave initiated by the debris cloud impact causes limited spalling to the rear of the substructure, between $X = 3.4$ and 6.6 mm. These damage mechanisms combine to produce the 9.8-mm hole shown in Fig. 6, which shows the computational results compared to a top-down view of specimen 17 substructure damage. The experimental and computational results shown in Fig 6 are shown to scale to allow comparison of the damage areas. The computational result shows only the intact portion of the substructure at 14.35 μs, with the debris cloud gases removed to make the substructure damage easier to discern.

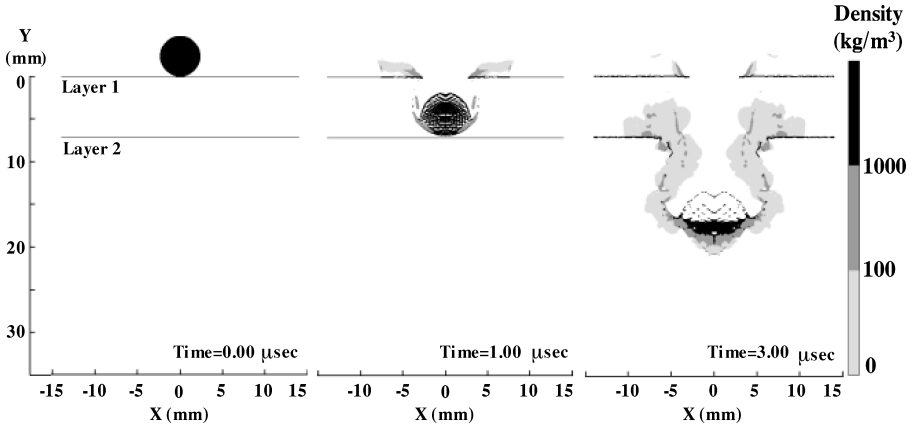

Fig. 4 Computational simulation of impact on all-titanium TPS panel during penetration of layers 1 and 2.

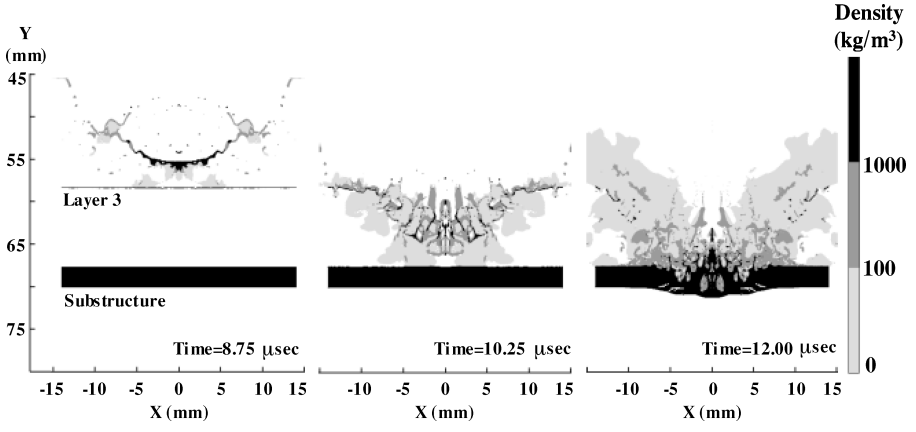

Fig. 5 Computational simulation of impact on all-titanium TPS panel during penetration of layer 3 and substructure.

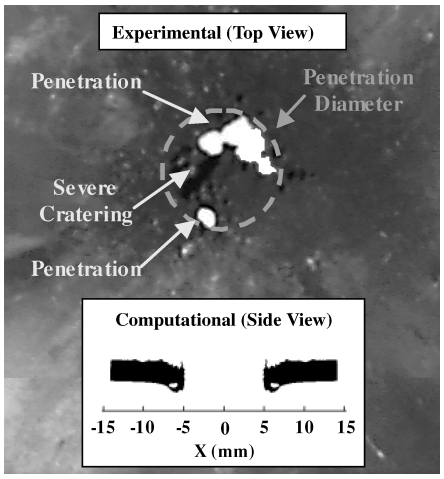

Fig. 6 Comparison of predicted and measured substructure damage for all-titanium TPS panel.

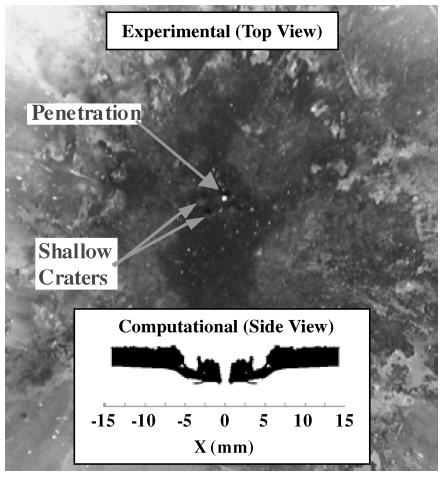

Fig. 7 Comparison of predicted and measured substructure damage for Inconel TPS panel.

Substructure penetration in specimen 17 appears to be due to multiple overlapping fragments. When fragment impacts partially overlap multiple craters are formed, one on top of the other. This buildup of damage can result in penetration even if the individual fragments do not have sufficient energy to penetrate the substructure alone. There are two distinct holes in the experimental substructure. The larger hole measures 10.5 by 4.4 mm and the smaller hole measures 2.5 by 1.4 mm. There is an area of severe cratering between the two holes formed by multiple small fragment impacts. Both holes and the severely cratered area are located within a diameter of 15 mm, labeled penetration diameter in Fig. 6. Several less severe fragment craters are located outside of the penetration diameter drawn on Fig. 6. A barely visible bulge is also noticed in the substructure.

Similar phenomena are observed when comparing specimen 17 to the corresponding computational result. Penetration by multiple small fragments occur in both experiment and computation. Regions of fragment overlap are observed in computation, as well as experiment. The area of significant damage to the experimental substructure, labeled the penetration diameter in Fig. 6 has a diameter of 15 mm, which is comparable to the calculated penetration diameter of 9.8 mm. It is not clear why two distinct substructure penetrations occurred in the experiment. This indicates that there were two separate mass concentrations in the debris cloud, which may be due to debris cloud interaction with the honeycomb core, but could also be due to breakup of the projectile before impact with the outer facesheet of the outer honeycomb sandwich. Premature projectile breakup is a commonly observed occurrence in hypervelocity impact testing. It is hypothesized that if the mechanism resulting in distinct damage regions was not present in the experiment, the experimental substructure penetration diameter would be smaller and would compare more favorably with the computational results.

To aid in discussion of the experimental and computational results, several limitations of axisymmetric models should be noted. The first limitation is that fragments away from the impact centerline have a cylindrical annulus shape. Thus, if a off-centerline fragment penetrates the substructure, it results in a annular hole, separating the substructure material in the center from the rest of the substructure. Thus, the predicted substructure damage characteristics may differ from experiment. However, the computational results should give a good indication of the degree of dispersion and state of the material in the debris cloud.

The second computational model is of a TPS panel using Inconel 617 outer honeycomb sandwich, generated for comparison with experimental specimen 6. Experimental parameters are listed in Table 1. Except for the omission of honeycomb core and Saffil insulation layers, the computational parameters are the same as the experimental parameters. The progression of impact in the second model is qualitatively similar to the computational results shown for the all-titanium model in Figs. 4 and 5 and is not shown. The second model significantly overpredicts substructure hole size, as shown in Fig. 7. Computational results are shown at 16.5 μs. Only intact portions of the substructure are shown, with impact debris removed to allow substructure damage to be seen clearly. Although the centerline fragment penetration diameter of 0.8 mm compares favorably with the experimental hole diameter of 0.7 mm, it is clear that if this calculation were run for a longer time that the significant fragment crater at $X = 4.5$ mm would result in the substructure region at $X > 4.5$ mm becoming detached, resulting in a computed hole size of 10.3 mm. Experimentally, only one fragment penetration occurred, along with several shallow fragment craters.

The reason for the lack of agreement between computation and experiment is unclear and may be due to the lack of required material properties for Inconel 617. Omission of the honeycomb core and Saffil insulation layers in the computational model also may have affected the predicted substructure damage. There are also unknowns associated with the experiment. It is possible that, in the experiment, the particular impact location relative to the foil walls in the honeycomb core increased dispersion of the impacting projectile, resulting in less substructure damage. It is also possible that the projectile broke up prematurely in the experiment, which could lead to less substructure damage.

Although substructure damage is overpredicted in the second model, TPS with Inconel 617 outer honeycomb sandwich is of primary interest in this research and is used in the statistical sensitivity analysis that follows. It is assumed that the Inconel model will produce results that are trendwise accurate, allowing TPS parameter variations to be ranked according to influence on protection provided to underlying components.

Statistical Sensitivity Analysis

The primary objective of this study is to determine the most effective place to make minor design changes to an existing metallic TPS to improve hypervelocity impact protection. The effects of a large number of parameters, or factors, needed to be quantified and compared. An efficient method was needed to assess the relative importance of many factors. The conventional approach would be to investigate one factor at a time, with the remaining factors held constant. This method is acceptable for a few variables that do not change much from their baseline values. Moreover, this one-factor-at-a-time method assumes that the effect of each variable is independent of variations of the other variables.

A factorial design approach can be used in which a few discrete values are chosen for each design parameter, and all possible combinations are evaluated. However, the number of analyses required can quickly become unmanageable.

The method selected for this study borrows techniques commonly used in robust design.[13,14] Design parameters (independent variables) are varied simultaneously in a matrix of experiments (or in this case, a matrix of analyses) defined by orthogonal arrays. The

effects of a large number of design parameters, evaluated over the range of interest, can be determined efficiently using this method. The method used in this study follows closely the procedures presented in Ref. 13, as well as similar procedures in Ref. 14.

The first step in statistical sensitivity analysis is to identify the design parameters of interest. Care must be taken to select a reasonable and meaningful range of variation for each design parameter. The range of variation can affect how much each factor influences the results. The selection of the factors and their ranges usually depends on engineering experience and judgment, and a good selection is essential to formulate the problem properly for meaningful results. Several levels, usually two to four, are selected to cover the range of each design parameter.

The next step in statistical sensitivity analysis is to determine what experiments or analyses need to be performed to determine the effects of the selected factors on the performance of the system. Orthogonal arrays are used to define the number of analyses to be performed and the combination of design parameter levels for each analysis. A limited number of standard orthogonal arrays[14] are available to accommodate specific numbers of design parameters with various levels per design parameter. Table 3 shows the L_{16} two-level orthogonal array used in this paper. In the orthogonal array there is a column for each design parameter, and each row is a particular combination of levels of each design parameter. The numbers 1 and 2 in Table 3 represent the level of a particular design parameter in a given analysis. The columns of the array are mutually orthogonal that is, for any pair of columns, all combinations of design parameter levels occur, and they occur an equal number of times.[13] The smallest standard orthogonal array is chosen to accommodate the number of design parameters and design parameter levels. Any extra columns in the orthogonal array can either be ignored, or in some cases used to estimate the effects of interactions between design parameters.

An experiment, or in this case an analysis, is performed for every row in the orthogonal matrix with the combination of design parameter levels defined in that row. Interpretation of the results is straightforward. The result or results for each analysis are tabulated, and the overall means for all analyses are calculated. The means for each level of every design parameter are also calculated. Each column of the orthogonal matrix contains an equal number of experiments at each level of the design parameter associated with that column. The results associated with each level of that design parameter are averaged to obtain the associated means. The effect of a design parameter level is defined as the deviation it causes from the overall mean. Therefore, the effect of each design parameter level can be obtained by subtracting the overall mean from the mean associated with the particular level of that design parameter. This process of estimating the design parameter effects is sometimes called analysis of means (ANOM).

When ANOM is used, the effect of each design parameter, called the main effects, can be determined independently. A simple additive or superposition model is assumed for the response η:

$$\eta = \text{overall mean} + \sum_{\substack{\text{design}\\ \text{parameter}}} (\text{design parameter effect}) + \varepsilon \qquad (1)$$

where ε is the error of the additive approximation. Thus, the response for any combination of design parameter levels can be estimated using this equation. In a typical design of experiments analysis, this error term would also include a contribution associated with the error in repeatability of measuring η for a given experiment. However, for the current application the response is obtained from analysis, so error associated with measurement repeatability does not exist.

The results of ANOM can provide considerable insight into the effect of the various design parameters; however, an analysis of variance (ANOVA) can give a more accurate indication of the relative importance of the design parameters and provides a means of ranking the factors in order of importance. ANOVA can be used to determine the contribution of each design parameter to total variation from the overall mean value. The sum of squares of the differences from the mean for all of the levels of a particular design parameter provides a measure of how much that design parameter affects the result over the specified range. The percentage that this sum of squares value contributes to the total for all design parameters gives a measure of the relative importance of that particular design parameter.

As part of the ANOVA, the error associated with the additive assumption can be estimated. The method used for the error estimate depends on the number of design parameters and design parameter levels and on the orthogonal matrix used in the statistical sensitivity analysis.

The sum of squares due to error[13] can be calculated using the following relationship:

$$\begin{aligned}\text{sum of squares due to error} = {} & (\text{grand total sum of squares})\\ & - (\text{sum of squares due to mean})\\ & - (\text{sum of squares due to design parameters})\end{aligned} \qquad (2)$$

where the grand total sum of squares is the sum of the squares of all values for a particular result, the sum of squares due to the mean is the overall mean squared times the number of analyses (or number of rows in the orthogonal matrix) and the sum of squares due to design parameters is the sum of squares of all of the design parameter effects. There are degrees of freedom associated with each of the quantities in Eq. (2). The degrees of freedom for the grand total sum of squares are the number of rows in the orthogonal matrix. There

Table 3 L_{16} two-level orthogonal array

	Design parameter														
Trial number	A	B	$A\times B$, $C\times D\times E$	C	$A\times C$, $B\times D\times E$	$B\times C$, $A\times D\times E$	$D\times E$, $A\times B\times C$	D	$A\times D$, $B\times C\times E$	$B\times D$, $A\times C\times E$	$C\times E$, $A\times B\times D$	$C\times D$, $A\times B\times E$	$B\times E$, $A\times C\times D$	$A\times E$, $B\times C\times D$	E
1	1	1	1	1	1	1	1	1	1	1	1	1	1	1	1
2	1	1	1	1	1	1	1	2	2	2	2	2	2	2	2
3	1	1	1	2	2	2	2	1	1	1	1	2	2	2	2
4	1	1	1	2	2	2	2	2	2	2	2	1	1	1	1
5	1	2	2	1	1	2	2	1	1	2	2	1	1	2	2
6	1	2	2	1	1	2	2	2	2	1	1	2	2	1	1
7	1	2	2	2	2	1	1	1	1	2	2	2	2	1	1
8	1	2	2	2	2	1	1	2	2	1	1	1	1	2	2
9	2	1	2	1	2	1	2	1	2	1	2	1	2	1	2
10	2	1	2	1	2	1	2	2	1	2	1	2	1	2	1
11	2	1	2	2	1	2	1	1	2	1	2	2	1	2	1
12	2	1	2	2	1	2	1	2	1	2	1	1	2	1	2
13	2	2	1	1	2	2	1	1	2	2	1	1	2	2	1
14	2	2	1	1	2	2	1	2	1	1	2	2	1	1	2
15	2	2	1	2	1	1	2	1	2	2	1	2	1	1	2
16	2	2	1	2	1	1	2	2	1	1	2	1	2	2	1

is one degree of freedom associated with the mean. Each design parameter has one less degree of freedom than the number of levels for that design parameter. Therefore, the degrees of freedom for the error can be calculated as follows:

(degrees of freedom for error)
= (number of rows in orthogonal matrix − 1)
− (sum of degrees of freedom for all design parameters) (3)

The degrees of freedom for the error must be greater than zero for Eq. (2) to be useful.

An approximate estimate of the sum of the squares due to error can be obtained by pooling the sum of squares corresponding to the design parameters having the lowest mean square. A rule of thumb[13] is to use the sum of squares corresponding to the bottom-half of the design parameters (as defined by lower mean square) and the degrees of freedom corresponding to those design parameters. Pooled error estimates are used for the results shown in this paper.

Once the sum of square due to error and the degrees of freedom for error have been calculated, the error variance can be estimated as follows:

$$\text{error variance} = \frac{\text{(sum of squares due to error)}}{\text{(degrees of freedom for error)}} \tag{4}$$

The variance ratio F is a measure of how important the effects of a design parameter are compared to the error.

$$F = \frac{\text{(mean square due to a factor)}}{\text{(error variance)}} \tag{5}$$

The mean square due to a design parameter is the sum of squares of the differences from the mean for a design parameter divided by the degrees of freedom associated with that design parameter.

Design Parameters

In all sensitivity analyses, a 0.476-cm-diam Al 1100-O projectile was assumed with a normal impact velocity of 7.1 km/s. From a series of experimental impacts on metallic TPS,[3] it was found that 0.318-cm-diam aluminum projectiles could be stopped by most TPS configurations without modification. All tests with 0.635-cm-diam aluminum projectiles resulted in penetration of the TPS and substructure, and it was clear from the level of damage that significant modification of the TPS would be required to provide protection against projectiles of this size. However, substructure damage in tests with 0.476-cm-diam aluminum projectiles was very sensitive to changes in TPS parameters, making this projectile size interesting for study in a sensitivity analysis. It seems likely that minor modifications to the TPS design will improve impact resistance to projectiles in this size range.

The thicknesses of each of the three layers, as well as the spacing between layers 1 and 2 and the spacing between layers 1 and 3, were selected as design parameters. Table 4 lists the five design parameters, A–E, along with the design parameter levels studied.

Levels were chosen that would encompass a reasonable design range for metallic TPS panels. In addition, design parameters A–C were calculated so that the difference in mass between level 1 and 2 would be the same for each, 0.05 kg per panel (0.54 kg/m^2). This is to determine the most effective location in the TPS to add mass. Level 1 and level 2 values for design parameters D and E were chosen to encompass a design range reasonable for metallic TPS panels and do not represent equal mass differences in a simple way. The change in mass for parameter D is dependent on the density of the honeycomb core. For the honeycomb used in the experiments,[15] a 0.71-cm increase in honeycomb thickness results in a 0.95-kg/m^2 weight increase. The change in mass for parameter E is dependent on the specific metallic TPS design being used and the method of varying the standoff between layers 1 and 3. The following discussion will focus on the metallic TPS panel design shown in Fig. 1. For reference, the areal mass of the baseline TPS configuration (parameters as specified for experiment 6 in Table 1) is 7.13 kg/m^3. This is based on design equations from Ref. 15, modified to account for the lower density insulation used in the experiments. If the insulation thickness is increased and the beaded side wall elongated to accommodate the 2.54-cm increase in overall TPS thickness between levels 1 and 2 of design parameter E, the weight increase, calculated using data from Ref. 15, is 0.88 kg/m^2. However, the increase in insulation weight accounts for 70% of this weight and is not required. With modification, the TPS panel could be constructed with a spacer underneath the insulation layer that would allow TPS panel thickness to be varied without increasing insulation thickness, potentially reducing the weight increase related to parameter E. There are, however, other less obvious weight penalties related to increasing the TPS panel thickness. Increasing design parameter E from level 1 to level 2 significantly effects the outer mold line of the vehicle, so that the impact on vehicle weight or performance will be greater than just the TPS weight increase.

Table 4 Parameter levels studied in statistical sensitivity analysis

Design Parameter	Level 1, cm	Level 2, cm	Description
A	1.27E−02	1.91E−02	Thickness layer 1
B	1.27E−02	1.91E−02	Thickness layer 2
C	7.62E−03	1.96E−02	Thickness layer 3
D	7.11E−01	1.42E+00	Spacing layer 1/layer 2
E	5.79E+00	8.33E+00	Spacing layer 1/layer 3

Orthogonal arrays are used to define the number of analyses to be performed and the combination of design parameter levels for each analysis. A limited number of standard orthogonal arrays are available to accommodate specific numbers of design parameters with various levels per parameter.[14] An L_{16} two-level orthogonal array, shown in Table 3, was selected for statistical sensitivity analysis since in this case it provides high resolution for the determination of design parameter sensitivity. The L_{16} array contains 15 columns and requires 16 experiments or analyses to be performed. Design parameters can be assigned to certain columns dependent on the orthogonal array chosen. In this study, the 2nd, 3rd, 5th, 9th, and 16th columns were used for design parameters A–E. A signal strength, which can be thought of as a signal-to-noise ratio, is calculated for each column to reveal the system sensitivity to variation of the design parameters. Signals are also obtained for interactions between the design parameters. The other columns in Table 3 contain interactions between the design parameters, where $\times$ represents interaction. For example, $A \times B$, located in column 3, represents the interaction between design parameters A and B. The columns containing interactions are confounded, meaning that multiple readings are contained in the same column. In this case, each double interaction is confounded with a triple interaction. In the preceding example, the fourth column contained the interaction between design parameters C, D, and E in addition to the interaction between design parameter A and B. Predicted sensitivities will be less accurate for interactions because columns with interactions are confounded. The emphasis of this research is on the effect of design parameter variation, and the design parameters were found to be more influential than the interactions. Each row represents a particular analysis, where the 1 and 2 entries in the remaining columns represent the design parameter levels. As shown in Table 3, there are 16 rows, trials 1–16, where each row represents a single analysis. The numbers in the row, either 1 or 2, represent the level of the design parameters for the analysis. Numbers listed in columns containing interactions are used in interpretation of the results and have no influence on the design parameter levels analyzed.

Damage Metrics

Use of statistical analysis requires identification of a response η to be measured as a factor of goodness, a way of quantifying the positive effect of varying design parameters. Careful selection of this factor is essential to obtaining meaningful results, and the parameter chosen should directly represent the physics involved in the process.[14]

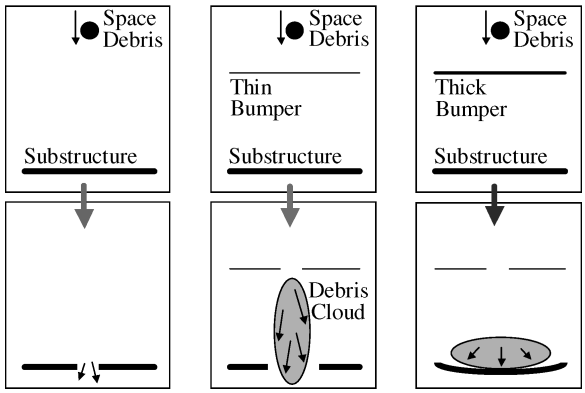

Fig. 8 Schematic representation of hypervelocity impact with three different conceptual shielding configurations.

In this study, η relates to the effectiveness of the TPS at protecting components located underneath the TPS, such as the aluminum substructure in the experiments. It is a measure of the damage potential to the substructure, or in other words, a damage metric. Two forms of damage metrics were investigated: predicted substructure damage and degree of dispersion of the incoming projectile.

Predicted substructure damage using hole sizes was the more intuitive damage metric; however, statistical analysis using substructure hole size as a factor of goodness produced misleading results when used with statistical sensitivity analysis. Figure 8 shows three conceptual impact cases that reveal why this is the case. The first case (Fig. 8a) shows impact on an unprotected substructure, resulting in a hole approximately the size of the incoming projectile. The second case (Fig. 8b) uses a Whipple shield that results in projectile breakup, but does not sufficiently disperse the projectile debris cloud. The result is a substructure hole size that is larger than if the substructure was unprotected. Finally, the third case (Fig. 8c) represents an effective Whipple shield that disperses the debris cloud to the extent that the substructure withstands the impact. If these shield designs were ranked based on substructure hole size the no bumper design (Fig. 8a) would be ranked above the thin bumper design (Fig. 8b), even though the thin bumper design is reducing and dispersing the impact energy. Statistical sensitivity analysis based on a metric related to substructure hole size will not produce meaningful results.

The other form of damage metric identified focuses on the degree of dispersion of the incoming projectile. In this form of damage metric, the state of the projectile debris cloud after impact with TPS, before substructure impact, is used. Identification of a single number that would adequately describe the degree of debris cloud dispersion was difficult. It was decided to measure what will be referred to as percent momentum radius for several different percentage values. Percent momentum radius is defined as the radius, measured from the axis of symmetry, that contains a specified percentage of the initial projectile axial momentum. This concept is shown in Fig. 9 for a highly idealized impact scenario, where 50 and 100% momentum radii are shown as a function of time. Percent momentum radius is a time-dependent quantity, which requires that a consistent reference be used for measurement in all of the cases examined. Because the geometry of the cases varied considerably, a fixed time was not used, for example, 10 μs. Instead, percent momentum radius was recorded at the initiation of substructure impact, which varied from 10 to 16 μs after initial projectile impact.

Percent momentum radius was calculated over the active computational cells only. To improve runtime and eliminate potential numerical problems, the computational cells containing layers 1 and 2 were removed after impact. In addition, momentum was lost out of the sides of the computational domain, which was sufficiently dispersed to be of no threat to the substructure, but does result in a significant drop in total momentum. Because of these momentum losses, the largest percent momentum that could be used for all cases was 30%. In addition, 10 and 20% momentum radii were calculated.

Table 5 Damage metric data for statistical sensitivity analyses

	Damage metric			
Trial number	Hole diameter, cm	10% Momentum radius, cm	20% Momentum radius, cm	30% Momentum radius, cm
1	1.24	0.33	0.441	0.61
2	0.75	0.24	0.416	0.65
3	0.136	0.43	0.6	0.74
4	0.16	0.24	0.333	0.47
5	1.76	0.56	0.708	0.83
6	0.62	0.24	0.429	0.49
7	0.2	0.41	0.518	0.61
8	0.34	0.30	0.568	1.07
9	0.17	0.59	0.708	0.89
10	0.66	0.23	0.473	0.64
11	0.04	0.42	0.511	0.67
12	0.17	0.30	0.778	1.41
13	1.26	0.40	0.518	0.73
14	0.156	0.46	0.873	1.28
15	0.079	0.49	0.67	0.9
16	0.58	0.30	0.575	0.76

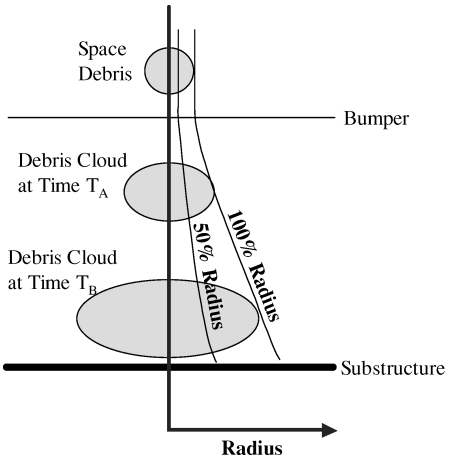

Fig. 9 Explanation of percent momentum radius using idealized diagram of axisymmetric impact problem; debris cloud at several arbitrary times.

Percent momentum radius was used in preference to substructure hole size because it was more directly related to the physics of projectile breakup. Use of this parameter resulted in the ranking of TPS designs based on their ability to disperse incoming projectiles, which has the added advantage of uncoupling the computational results for the TPS from the specific substructure material and geometry simulated.

Results

TPS Design Guidelines

After completing the analyses specified in Table 3, statistical sensitivity analysis was performed for several different damage metrics. Table 5 lists the predicted substructure hole size and momentum radii. All simulations predict substructure penetration, however, improvement in debris cloud dispersion is achieved through variation of the TPS parameters. Table 6 shows representative ANOVA results for the 30% momentum radius damage metric. Design parameters and interactions (columns from Table 3) are listed in order of influence to the damage metric. Design parameter E has the most effect on the 30% momentum radius damage metric. The second column in Table 6 lists a description of the design parameters. For example, design parameter E is the spacing between layers 1 and 3. The third and fourth columns list the difference from mean of the damage metric at design parameter levels 1 and 2, respectively. In this case, design parameter E results in an average -0.17-cm decrease in the 30% momentum radius when set to 5.79 cm and a 0.17-cm increase

Table 6 ANOVA for 30% momentum radius damage metric

Parameter	30% Momentum radius factor ranking	Difference from mean, cm		Sum of squares (SS)	% Total SS	DOF	Mean SS	F
		Level 1	Level 2					
E	Spacing layer 1/layer 3	$-1.74E{-}01$	$1.74E{-}01$	$4.87E{-}01$	46.49	1	$4.87E{-}01$	46.06
A	Thickness layer 1	$-1.13E{-}01$	$1.13E{-}01$	$2.05E{-}01$	19.56	1	$2.05E{-}01$	19.39
$D \times E$	Interaction	$8.19E{-}02$	$-8.19E{-}02$	$1.07E{-}01$	10.25	1	$1.07E{-}01$	10.15
$A \times D$	Interaction	$6.31E{-}02$	$-6.31E{-}02$	$6.38E{-}02$	6.09	1	$6.38E{-}02$	6.04
D	Spacing layer 1/layer 2	$-4.94E{-}02$	$4.94E{-}02$	$3.90E{-}02$	3.73	1	$3.90E{-}02$	3.69
$C \times D$	Interaction	$4.94E{-}02$	$-4.94E{-}02$	$3.90E{-}02$	3.73	1	$3.90E{-}02$	3.69
B	Thickness layer 2	$-3.69E{-}02$	$3.69E{-}02$	$2.18E{-}02$	2.08	1	$2.18E{-}02$	2.06
$A \times E$[a]	Interaction	$3.56E{-}02$	$-3.56E{-}02$	$2.03E{-}02$	1.94	1	$2.03E{-}02$	
C[a]	Thickness layer 3	$-3.19E{-}02$	$3.19E{-}02$	$1.63E{-}02$	1.55	1	$1.63E{-}02$	
$B \times C$[a]	Interaction	$-3.06E{-}02$	$3.06E{-}02$	$1.50E{-}02$	1.43	1	$1.50E{-}02$	
$A \times B$[a]	Interaction	$-2.94E{-}02$	$2.94E{-}02$	$1.38E{-}02$	1.32	1	$1.38E{-}02$	
$C \times E$[a]	Interaction	$2.69E{-}02$	$-2.69E{-}02$	$1.16E{-}02$	1.10	1	$1.16E{-}02$	
$B \times D$[a]	Interaction	$1.69E{-}02$	$-1.69E{-}02$	$4.56E{-}03$	0.44	1	$4.56E{-}03$	
$B \times E$[a]	Interaction	$1.19E{-}02$	$-1.19E{-}02$	$2.26E{-}03$	0.22	1	$2.26E{-}03$	
$A \times C$[a]	Interaction	$-6.87E{-}03$	$6.87E{-}03$	$7.56E{-}04$	0.07	1	$7.56E{-}04$	
Total				$1.05E{+}00$	100			

[a]Pooled error, $8E{-}02$ SS, 8-DOF, $1E{-}02$ mean SS.

Table 7 Recommended change in design parameters determined using different damage metrics

Rank	10% Momentum radius	20% Momentum radius	30% Momentum radius
1	Decrease D	Increase E	Increase E
2	Increase E	Increase A	Increase A

when set to 8.33 cm. The fifth and sixth columns report the sum of squares of the damage parameter and percent total of the sum of squares. The seventh column lists the degrees of freedom (DOF) of each design parameter and interaction, which is 1 in all cases because the array is limited to two levels. The eighth column is the mean sum of squares, which was calculated by dividing the sum of squares by the number of DOF.

The final step in statistical sensitivity analysis is to calculate the variance ratio F. The variance ratio, similar to a signal-to-noise ratio, measures the importance of the effects of a design parameter compared to the error or noise in the results. The variance ratio F, calculated using Eq. (5), is shown in the ninth column of Table 6.

Table 7 lists the two most influential design parameters for each of the damage metrics examined. Statistical sensitivity analyses using 20 and 30% momentum radii both predict that a 2.54-cm variation of design parameter E will have the most influence on debris cloud dispersion. The second most influential design change was the 0.00635-cm variation of design parameter A. Both the 20 and 30% momentum radii predict that increasing the value of parameters E and A will increase debris cloud dispersion and, it is assumed, provide better protection from hypervelocity impacts to the underlying components.

Even though it is predicted that design parameter E is more influential than design parameter A, it is likely that from a design standpoint design parameter A is the better parameter to change. Change of design parameter E, although more influential than changing A, results in a 0.88-kg/m^2 increase in TPS weight, whereas the increase of parameter A from level 1 to level 2 results in a 0.54-kg/m^2 increase in TPS weight. Although modifications could be made to the TPS design to reduce the weight increase associated with increasing parameter E, increasing the thickness of the TPS panel influences the outer mold line of the vehicle, which will have a negative effect vehicle weight and performance. Increasing design parameter A, the outer facesheet thickness, provides additional benefits to the vehicle from an operability standpoint. Increasing the outer facesheet thickness increases the ability of the vehicle to fly through rain, resist ground hail strikes, and resist damage during assembly.

Further examination of Table 7 reveals that there is a discrepancy between predictions using 10% momentum radius as a damage metric and those using larger radii, such as 20% momentum radius and 30% momentum radius. Although there is agreement that design parameter E is influential, using the 10% momentum radius damage metric results in the prediction that a 0.71-cm variation in design parameter D, the spacing between layers 1 and 2, is the most influential and that the value of the parameter should be decreased to improve impact protection. This nonintuitive result leads to the hypothesis that there are some phenomena leading to the difference of predictions resulting from using 10% momentum radius as a damage metric, as opposed to the 20 or 30% momentum radius, and that the difference is probably related to the fact that 10% momentum radius measurements focus on a narrower region of the impact debris cloud than 20 and 30% momentum radii measurements. Analysis results were examined to obtain a better understanding of the phenomena leading to this discrepancy and are discussed in the following section.

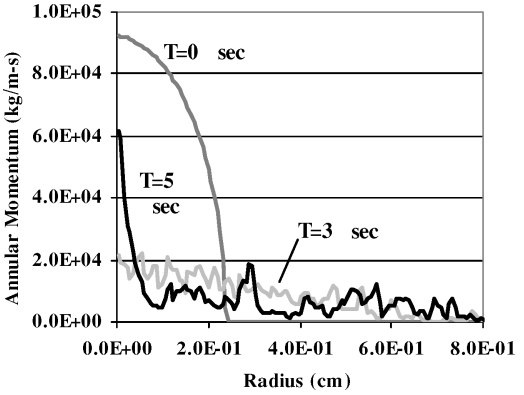

Fig. 10 Annular momentum distribution in typical axisymmetric simulation, revealing centerline mass accumulation after impact with layer 2.

Modeling Artifacts

Examination of density and momentum data during the penetration of layer 2 reveals the source of discrepancy between the 10% momentum radius damage metric, which focuses on a narrow region of the computational domain, and the 20 and 30% damage metrics, which focus on a larger area. Momentum readings along the axis of symmetry were found to decrease gradually after impact with layer 1, as expected, but after impact with layer 2 momentum along the centerline increases rapidly. This is shown in Fig. 10, which plots annular momentum per unit area at 0.0, 3.0, and 5.0 μs for a typical impact simulation. Annular momentum per unit area is defined in Fig. 11 and is

$$L_{\text{annular}}(i) = \sum_{j=1}^{n} \frac{L(i,j)}{A(i)} \tag{6}$$

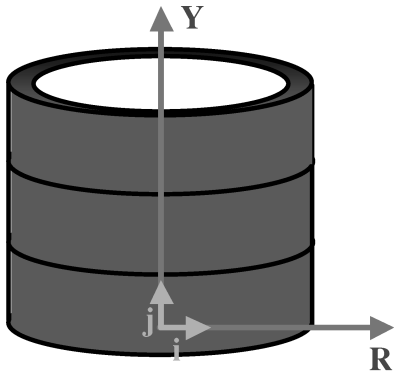

Fig. 11 Schematic showing the summation of axial momentum in annular elements, where $L(i, j)$ is the axial momentum of annular element at radial indice i and axial indice j.

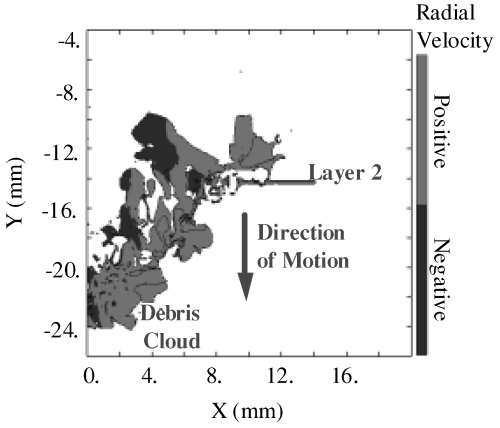

Fig. 12 Initiation of funnel effect during penetration of layer 2.

where i and j are the radial and axial computational cell indices, L is the axial momentum of the specified cell, and A is the cross-sectional area of the annulus formed by the computational cell at the specified radial index. At $T = 0.0$ μs, impact is initiated with layer 1. At $T = 3.0$ μs, penetration of layer 2 is in progress, and the annular momentum has decreased substantially. However, at $T = 5.0$ μs, after penetration of layer 2, a spike is noticeable in the annular momentum at radius of 0.0 cm, along the axis of symmetry. Examination of debris cloud radial velocity during penetration of layer 2 revealed that as layer 2 deforms it imparts a significant negative radial velocity to portions of the debris cloud, as shown in Fig. 12. This funnel effect directs portions of the debris cloud to the axis of symmetry. In the axisymmetric model used, the radial velocity of the funneled debris is set to zero when it reaches the axis of symmetry, causing debris to accumulate along the axis. The funnel effect combined with the centerline mass accumulation results in the increase of momentum along the centerline.

Estimation of the upper bound value of centerline mass accumulation reveals from 0 to 4% of the initial axial momentum concentrated along the centerline after impact with layers 1 and 2, where extent of momentum concentration depends on the configuration of layer 1, layer 2, and the spacing between these layers. The funnel effect and centerline mass accumulation explains the discrepancy between the statistical sensitivity analysis results using 10% momentum radius and sensitivity analyses using larger momentum radii. Because centerline mass accumulation may be as high as 4%, the 10% momentum radius will be significantly influenced, where the degree of influence will be lower for 20 and 30% momentum radii.

Conclusions

A design of experiments approach was used with computational hypervelocity impact analyses to determine the most effective place to make minor changes to an existing metallic TPS design to improve hypervelocity impact protection to underlying components. This study is conducted at a preliminary design level, focusing on general improvements to the hypervelocity impact protection behavior of the TPS, without specification or detailed modeling of the underlying components that would be necessary at a final design level. The underlying component to which the TPS attaches could include fuel tanks, crew cabins, or structural members. In addition to the TPS, a 0.254-cm-thick aluminum 2024-T81 plate is included in the model, located directly underneath the TPS. The aluminum plate is representative of the space shuttle substructure and is included in the model to allow comparison with experimental results.[3]

Two axisymmetric models were created for comparison with two experimental impact test configurations reported in Ref. 3. The first configuration uses a Ti–6Al–4V outer honeycomb sandwich panel, and the second configuration uses a Inconel 617 outer honeycomb sandwich panel. Several modeling assumptions and simplifications were required and are reported, The axisymmetric models predict that penetration of the representative space shuttle substructure is primarily due to solid fragments remaining in the debris cloud, which is consistent with experimental results. The predicted substructure penetration diameter for the first configuration, 9.8 mm, was comparable to the 15-mm diameter of the circle that encloses the area of substructure penetration and significant cratering in the experiment. Penetration diameter for the second configuration was significantly larger than the corresponding experiment penetration. Possible explanations for discrepancies are given for both configurations.

The second TPS configuration, which uses a Inconel 617 outer honeycomb sandwich panel, was of primary interest and was selected for use in the statistical sensitivity study. Five TPS parameters were studied. The choice of appropriate damage metric, used as a factor of goodness to rank competing designs, was critical. Use of percent momentum radius as a damage metric provides a good indication of the level of dispersion of the hypervelocity projectile before impact with the substructure. Use of 20 or 30% momentum radii in sensitivity studies produced results that correspond to physical intuition. Of the design parameters investigated, increasing the spacing between the outermost layer and the substructure was predicted to be the most influential design change. The second most effective design change was to increase thickness of the outermost surface of the TPS panel. However, when other TPS design considerations are addressed, increasing the thickness of the outermost surface of the TPS panel has many advantages. Increasing the outer surface thickness not only improves hypervelocity impact protection, but also increases the resistance of the panel to rain, hail, and handling damage. On the other hand, increasing the spacing between the outermost layer and the substructure not only results in a greater increase of TPS weight but also adversely effects vehicle performance and weight by changing the outer mold line.

It was found that use of substructure hole size as a damage metric in statistical sensitivity analysis is misleading because the hole size does not directly indicate the level of dispersion in the debris cloud. This may result in marginally effective protection systems being ranked lower than the case of no protection system at all because the marginal systems will break up the hypervelocity projectile, potentially producing larger substructure holes.

The centerline mass accumulation observed in axisymmetric analysis results is not realistic for this problem. The discrepancy between 10% momentum radius sensitivity analysis results and the 20 and 30% momentum radii sensitivity results is attributed to the centerline mass accumulation. Use of 10% momentum radius as a damage metric produced unintuitive results because the focus of this measurement is the central portion of the model influenced by the centerline mass accumulation. It is concluded that 20 and 30% momentum radii measurements give a better indication of the degree of dispersion in the debris cloud.

In conclusion, a useful method has been developed for improving the hypervelocity impact protection provided by metallic TPS to underlying components. Analysis is performed at a preliminary design level with several simplifying assumptions. The results from sensitivity analyses provide guidance for future metallic TPS designs.

References

[1]Blosser, M. L., "Advanced Metallic Thermal Protection Systems for Reusable Launch Vehicles," Ph.D. Dissertation, Dept. of Mechanical and Aerospace Engineering, Univ. of Virginia, Charlottesville, VA, May 2000.

[2]Hertel, E. S., Jr., "Comparison of Analytic Whipple Bumper Shield Ballistic Limits with CTH Simulations," Sandia National Labs., Rept. SAND92-0347, Albuquerque, NM, May 1993.

[3]Karr, K. L., Poteet, C. C., and Blosser, M. L., "Hypervelocity Impact Test Results for a Metallic Thermal Protection System," NASA TM-2003-212440, Aug. 2003.

[4]McGlaun, J. M., Thompson, S. L., and Elrick, M. G., "A Brief Description of the Three-Dimensional Shock Wave Physics Code CTH," Sandia National Labs., Rept. SAND89-0607, Albuquerque, NM, July 1990.

[5]Poteet, C. C., "Computational Study of Hypervelocity Impacts on Metallic Thermal Protection Systems," M.S. Thesis, School of Engineering and Applied Science, George Washington Univ., Washington, DC, Aug. 1998.

[6]Anderson, E., Jr., "An Overview of the Theory of Hydrocodes," *International Journal of Impact Engineering*, Vol. 5, No. 1, 1987, pp. 33–59.

[7]Silling, S., "Use of the Johnson-Cook Fracture Model in CTH," Computational Physics and Mechanics Dept., Sandia National Labs., Albuquerque, NM, June 1996.

[8]Kerley, G. I., "Theoretical Equations of State for Aluminum," *International Journal of Impact Engineering*, Vol. 5, No. 3, 1987, pp. 441–449.

[9]Bell, R. L., Baer, M. R., Brannon, R. M., Elrick, M. G., Farnsworth, A. V., Hertel, E. S., Petney, S. V., Silling, S. A., and Taylor, P. A., "CTH User's Manual and Input Instructions," CTH Development Project, Sandia National Labs., Albuquerque, NM, July 1996.

[10]Babcock, S. G., Kumar, A., and Green, S. J., "Final Report on Response of Materials to Suddenly Applied Stress Loads. Part I: High Strain-Rate Properties of Eleven Reentry Vehicle Materials at Elevated Temperatures," General Motors Defense Research Labs., U.S. Air Force Dynamics Labs., AFFDL-TR-67-35, Pt. 1, Dayton, OH, April 1967.

[11]Klopp, W. D., "Inconel 617," *Aerospace Structural Metals Handbook*, Vol. 5, Center for Information and Numerical Data Analysis and Synthesis/U.S. Air Force Cooperative Research and Development Agreement Handbooks Operation, Purdue Univ., West Lafayette, IN, 1994, pp. 1–34.

[12]Hertel, E. S., Jr., Chhabildas, L. C., and Hill, S. A., "Whipple Bumper Shield Simulations," *Shock Compression of Condensed Matter 1991*, American Physical Society, Williamsburg, VA, 1991, pp. 987–990.

[13]Phadke, M. S., "Matrix Experiments Using Orthogonal Arrays," *Quality Engineering Using Robust Design*, Prentice–Hall, Englewood Cliffs, NJ, 1989, pp. 41–65.

[14]Ross, P. J., "Analysis and Interpretation Methods for Experiments," *Taguchi Techniques for Quality Engineering*, 2nd ed., McGraw–Hill, New York, 1996, pp. 91–179.

[15]Myers, D. E., Martin, C. J., Blosser, M. L., "Parametric Weight Comparison of Advanced Metallic, Ceramic Tile, and Ceramic Blanket Thermal Protection Systems," NASA TM-2000-210289, June 2000.

S. A. Bouslog
Associate Editor